Zigzag spin structure in layered honeycomb $Li_3Ni_2SbO_6$: A combined diffraction and antiferromagnetic resonance study

A. I. Kurbakov,[1,2,*] A. N. Korshunov,[1,2] S. Yu. Podchezertsev,[1] A. L. Malyshev,[1] M. A. Evstigneeva,[3] F. Damay,[4] J. Park,[5] C. Koo,[5] R. Klingeler,[5,6,†] E. A. Zvereva,[7] and V. B. Nalbandyan[3]

[1]*Petersburg Nuclear Physics Institute, NRC Kurchatov Institute, 188300 Gatchina, Russia*

[2]*Faculty of Physics, St. Petersburg University, 198504 St. Petersburg, Russia*

[3]*Chemistry Faculty, Southern Federal University, 344090 Rostov-on-Don, Russia*

[4]*Laboratoire Léon Brillouin, CEA Saclay, 91191 Gif-sur-Yvette, France*

[5]*Kirchhoff Institute of Physics, Heidelberg University, INF 227, 69120 Heidelberg, Germany*

[6]*Centre for Advanced Materials CAM, Heidelberg University, INF 225, 69120 Heidelberg, Germany*

[7]*Faculty of Physics, Moscow State University, 199991 Moscow, Russia*

(Received 7 April 2017; revised manuscript received 18 May 2017; published 12 July 2017)

The magnetic structure of $Li_3Ni_2SbO_6$ has been determined by low-temperature neutron diffraction, and the crystal structure has been refined by a combination of synchrotron and neutron powder diffraction. The monoclinic ($C2/m$) symmetry, assigned previously to this pseudohexagonal layered structure, has been unambiguously proven by peak splitting in the synchrotron diffraction pattern. The structure is based on essentially hexagonal honeycomb-ordered Ni_2SbO_6 layers alternating with Li_3 layers, all cations and anions being in an octahedral environment. The compound orders antiferromagnetically below $T_N = 15$ K, with the magnetic supercell being a $2a \times 2b$ multiple of the crystal cell. The magnetic structure within the honeycomb layer consists of zigzag ferromagnetic spin chains coupled antiferromagnetically. The ordered magnetic moment amounts to 1.62(2) μ_B/Ni, which is slightly lower than the full theoretical value. Upon cooling below T_N, the spins tilt from the c axis, with a maximum tilting angle of 15.6° at $T = 1.5$ K. Our data imply non-negligible ferromagnetic interactions between the honeycomb layers. The observed antiferromagnetic resonance modes are in agreement with the two-sublattice model derived from the neutron data. Orthorhombic anisotropy shows up in zero-field splitting of $\Delta = 198 \pm 4$ and 218 ± 4 GHz. Above T_N, the electron spin resonance data imply short-range antiferromagnetic order up to about 80 K.

DOI: 10.1103/PhysRevB.96.024417

I. INTRODUCTION

In recent years, synthesis and studies of new layered oxides of alkali and transition metals have attracted much attention, mostly for two different reasons: (i) the possibility of their use as electrode materials for lithium-ion or sodium-ion batteries and (ii) a rich variety of magnetic and electronic phenomena such as quasi-two-dimensional magnetism [1,2] with different types of spin ordering. Besides ternary LMO_2 compounds, there is a large family of honeycomb-ordered structures with tripled general formula $L_3M_2XO_6$; in some instances, L and X or L and M may be the same element, as in Li_2IrO_3 (i.e., $Li_3[Ir_2Li]O_6$) and in Li_5ReO_6 (i.e., $Li_3[Li_2Re]O_6$). The honeycomb arrangement of magnetic M cations provides a large variety of quantum ground states. Depending on the transition-metal ions, the Heisenberg-type Mott-insulator scenario which applies to 3d transition-metal-based systems is replaced by the description in terms of spin-orbit entangled Mott insulators for 4d and 5d elements. While the latter yields ground states like the Kitaev phase, a variety of different magnetic phases appears in the Heidelberg-like scenario too, such as Néel, stripy, zigzag, and different spiral orders [3–5]. Moreover, with the presence of strong lattice distortions or frustration of second- and third-neighbor magnetic interactions, ground states without long-range magnetic order could be realized [6,7], states demonstrating spin-gap behavior in particular [8–12].

The wide variety of magnetic structures and relevant magnetic properties of honeycomb layered oxides is largely caused by different relative arrangements of the layers, degree of inlayer ordering (i.e., the perfection of a honeycomb cation arrangement and distortions of the local surrounding of magnetic ions), the presence of stacking faults and their concentration, various types of alkali-metal coordination, and the distances between the honeycomb layers containing magnetic ions. Evidently, spin structure types and magnetic properties of honeycomb layered oxides are closely related to their crystal structures.

In the present work, $Li_3Ni_2SbO_6$ has been chosen for the structural investigation because it has been studied in detail with several methods [5,13], demonstrating its interesting and unusual magnetic properties, but its magnetic structure and the fine details of the crystal structure are unknown. Due to single-ion effects, the Ni^{2+} spins which form the hexagonal magnetic sublattice exhibit sizeable magnetic anisotropy, so that the Heisenberg scenario has to be extended by a small spin-orbit contribution. The laboratory XRD powder pattern of $Li_3Ni_2SbO_6$ might be indexed well with either a hexagonal or monoclinic cell. Based on the results of the Rietveld refinement, the monoclinic ($C2/m$) model was preferred, although peak splitting, which would be characteristic for low symmetry, was not observed [13]. The combination of

*Corresponding author: kurbakov_ai@pnpi.nrcki.ru

†Corresponding author: klingeler@kip.uni-heidelberg.de

 ©2017 American Physical Society

synchrotron and neutron powder diffraction methods used in the present work provides more detailed and unambiguous information owing to (i) the determination of the magnetic structure with neutrons, (ii) much better resolution of the synchrotron data, and (iii) better sensitivity of neutron diffraction to contributions from light atoms (O and Li). In addition, we have investigated the magnetic excitations by means of high-frequency and high-field electron spin resonance (HF-ESR) studies. The antiferromagnetic resonance modes are in agreement with the two-sublattice spin structure derived from the neutron data. The magnetic anisotropy is of the axial type. In addition, our data provide direct evidence for short-range antiferromagnetic order up to temperatures of about 5 times T_N.

II. EXPERIMENT

$Li_3Ni_2SbO_6$ was prepared with multistep solid-state reactions at the final temperature of 1150 °C followed by quenching as described earlier [13]. The characterization of the samples by means of magnetic susceptibility, specific heat, magnetization, *X*-band electron spin resonance, and nuclear magnetic resonance studies is reported elsewhere [5]. For the present neutron and synchrotron diffraction study, a larger batch was prepared from the same reagents by the same route, while for the HF-ESR the sample from Ref. [5] was used.

Neutron powder diffraction at room temperature (RT) was carried out on a sectional powder diffractometer SSPD located at the WWR-M reactor, Petersburg Nuclear Physics Institute (Gatchina, Russia). Monochromatic neutrons with wavelength 1.754 Å were produced using the Ge (004) reflection of the monochromator. Contamination of neutrons from the Ge (008) reflection of the monochromator was 0.3%. The sample was packed into a TiZr container (zero matrix) with an inner diameter of 8.5 mm, and neutron diffraction data were obtained in the 2θ range $4^\circ - 155^\circ$ with 0.1° steps. Instrumental parameters of the SSPD diffractometer were determined using the $Na_2Ca_3Al_2F_{14}$ standard.

Structural investigations at RT were carried out using high-resolution (an instrumental contribution to the FWHM of about 0.0035° at the minimum of the resolution function was estimated by fitting a standard Si diffraction pattern obtained before the measurements of the studied sample) x-ray powder diffractometer ID31 (this diffractometer has now moved to beamline ID22) at the European Synchrotron Radiation Facility (Grenoble, France). Monochromatic synchrotron radiation with a wavelength of 0.3999 Å was used. For this experiment, powder was sealed into a thin-walled borosilicate capillary with 0.7-mm inner diameter. The capillary was rotating during the measurements in order to exclude the influence of preferred orientation effects. Diffraction data were collected in the 2θ range from -12° to $+43^\circ$ with steps of 0.003°. The exact zero angle of the diffractometer was determined by comparing positions of the same reflections with positive and negative scattering angles. For Rietveld analysis, we used the diffraction pattern in the angular range from 4° to 43°. A standard silicon sample was measured before the experiment to obtain the instrumental function of the ID31 diffractometer.

The low-temperature neutron diffraction experiments were carried out on the cold neutron two-axis diffractometer G4.1 located at the Orphee reactor, Laboratory Léon Brillouin (Saclay, France). This diffractometer has a high luminosity (4×10^6 n cm^{-2}) in the entire angular range and a high resolution at low diffraction angles (the instrumental contribution to the FWHM amounts to about 0.25° at the minimum of the resolution function). The wavelength of the incident neutrons was 2.422 Å. The sample was encased in a vanadium container with an inner radius of 8 mm. Neutron diffraction data were collected in the 2θ range of $11^\circ - 91^\circ$ with steps of 0.1°. Measurements were carried out at the lowest reached temperature of 1.5 K, then at $T = 10$, 13, 14, 15, 16, 17, and 20 K. In order to compare the neutron diffraction patterns of the magnetically ordered and paramagnetic states, measurements at higher temperatures $T = 40$, 50, and 100 K were conducted. All diffraction patterns were treated with the Rietveld method using the FULLPROF suite [14,15].

HF-ESR measurements on the $Li_3Ni_2SbO_6$ polycrystal were performed by means of a phase-sensitive millimeter-wave vector network analyzer (MVNA) from ABmm as a stable source and detector of microwave radiation from 40 to 500 GHz. The external magnetic field for the magnetic resonance was applied by a 16/18 T superconducting magnet from Oxford Instruments. The experiment temperatures from 2 to 100 K were controlled in a variable-temperature insert by means of the ^{4}He flow and a resistive heater. The powder sample was loaded in a cylindrical waveguide probe [16].

III. RESULTS

A. Atomic structure

Results of the combined profile analysis of the synchrotron and neutron diffraction patterns at RT are shown in Fig. 1. Due to the high resolution of the ID31 beamline, diffraction peak splitting was revealed for the first time, unambiguously indicating that the true symmetry is monoclinic rather than hexagonal. Note that in the preceding work based on the laboratory XRD [13], the monoclinic $C2/m$ model was preferred only because of somewhat better agreement factors. In the present work, the $C2/m$ model has been confirmed and further refined.

The synchrotron pattern shown in Fig. 1(a) enables elucidating the crystal structure and determining the structural parameters which are listed in Tables I and II. The crystal structure of $Li_3Ni_2SbO_6$ is shown in Fig. 2. As our analysis shows strong *hkl*-dependent broadening of the diffraction peaks, the analysis considers both microstructural effects and *hkl*-dependent peak broadening. Note that the experimental data demonstrate a strong sloping background in the angular range of the superstructure peaks. This can be associated with stacking faults, which are a typical feature of honeycomb-ordered layered oxides [4–7,13,17–21].

Cooperative employment of the neutron and high-resolution synchrotron diffraction methods allows precise determination of the atomic coordinates and the occupancies of both heavy and light ions. Our joint refinement revealed the absence of Li/Ni mixed occupancy, which is observed in a number of related compounds and deteriorates the electrode activity in lithium-ion batteries. On the other hand, best-fit results were obtained with partial mixing of Sb and Ni

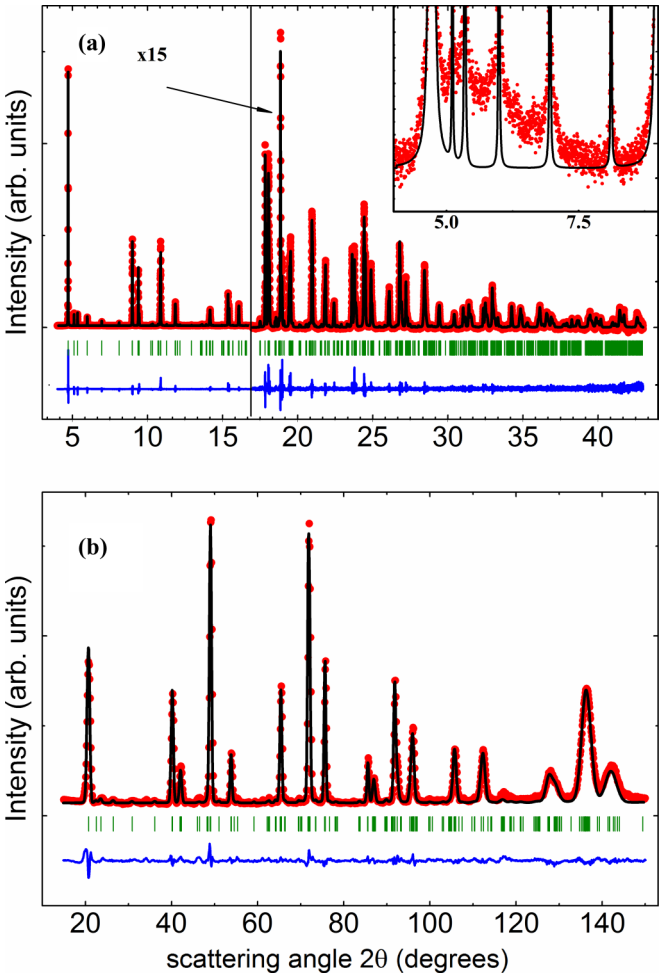

FIG. 1. Combined Rietveld refinement of RT synchrotron (ID31, $\lambda = 0.3999$ Å) (a) x-ray and (b) neutron (SSPD, $\lambda = 1.754$ Å) diffraction data for $Li_3Ni_2SbO_6$. Red dots represent the experimental data, black lines show the calculated intensity, blue lines indicate the difference between experimental and simulated data, and the green ticks show the Bragg reflections. The right-hand part of the synchrotron diffraction pattern is multiplied by a factor of 15. Inset: Small-angle region of the synchrotron diffraction pattern showing the anomalous background.

cations located at the 2a and 4g positions, respectively. In contrast, modeling the data without cation mixing leads to inappropriate results, i.e., (i) to an inadequate stoichiometry contradictory to the gross composition of the sample and (ii) abnormally low thermal parameters of the Ni cations. Hence, Ni^{2+}/Sb^{5+} mixing has to be considered in order to avoid these shortcomings. The results of the profile analysis are listed in Tables I and II.

However, random Ni^{2+}/Sb^{5+} mixing seems improbable due to their great difference in both oxidation states and ionic sizes. Thus, the value of cation mixing was fixed to be 10% concerning the 2a position, and stoichiometry of the compound was conserved. Most likely, the apparent Ni^{2+}/Sb^{5+} mixing is a fictitious effect resulting from stacking faults, whereas each individual layer is ordered. This apparent mixing is a typical feature of related honeycomb-layered structures ([4,6,20,21] and references therein). In contrast, in Cu^{2+} compounds such

TABLE I. Crystallographic data of $Li_3Ni_2SbO_6$ in the $C/2m$ (No. 12) space group at room temperature. Lattice constants $a = 5.18434(2)$ Å, $b = 8.97119(3)$ Å, $c = 5.16103(3)$ Å, $\beta = 109.7046(3)^\circ$, and $V_{cell} = 225.9821(15)$ Å^3. Agreement factors for synchrotron diffraction pattern are $R_p = 3.94\%$, $R_{wp} = 6.12\%$, $R_{exp} = 1.91\%$, and for the neutron diffraction pattern they are $R_p = 3.93\%$, $R_{wp} = 5.44\%$, $R_{exp} = 2.58\%$; global $\chi^2 = 7.35$. "U_{iso}" is the isotropic displacement parameter and "Occ." stands for occupancy.

Atom	Site	*x/a*	*y/b*	*z/c*	$10^2 \times U_{iso}$ (Å^2)	Occ.
Ni	4g	0	1/3	0	0.18(2)	0.95
Sb	4g	0	1/3	0	0.20(3)	0.05
Sb	2a	0	0	0	0.18(2)	0.9
Ni	2a	0	0	0	0.20(3)	0.1
O(1)	4i	0.7597(10)	0	0.2258(12)	0.085(3)	1
O(2)	8j	0.2365(8)	0.1564(4)	0.2332(7)	0.085(3)	1
Li(1)	4h	0	0.163(2)	1/2	0.59(2)	1
Li(2)	2d	0	1/2	1/2	0.59(2)	1

as $Na_2Cu_2TeO_6$ [8] and $Na_3Cu_2SbO_6$ [22], in which the honeycomb layers are far from hexagonal metrics due to the strong Jahn-Teller effect of Cu^{2+}, stacking disorder is prohibited, and apparent mixing is not observed.

A remarkable feature of the obtained high-resolution diffraction patterns is a significant broadening of the diffraction peaks in comparison to a standard silicon sample. To obtain the best match between calculated and experimental profiles, a phenomenological anisotropic peak-broadening model, namely, a monoclinic one, suggested by Stephens [23] and realized in the FULLPROF suite was applied. Peak shape analysis reveals that maximal strains propagate along the crystallographic *c* axis, indicating that stacking faults may influence the superstructure ordering in the studied compound. However, as seen in the inset of Fig. 1(a), this phenomenological approach, which takes into account the anisotropic broadening and inlayer cationic substitution, is not sufficient to fully describe the real crystalline structure. The accounting of an average structure, which is implicit in the framework of full-profile analysis, is not sufficient either. The description of the actual package of layers requires attraction of some additional methods of modeling of the stacking faults.

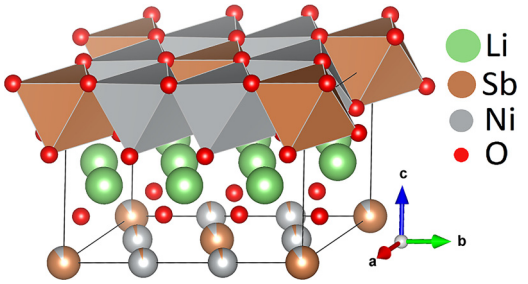

FIG. 2. Refined crystal structure of $Li_3Ni_2SbO_6$. Six NiO_6 octahedra surrounding one SbO_6 octahedron form honeycomb packed *ab* layers.

TABLE II. Selected interatomic distances and bond angles at room temperature.

Bond distances (Å)		Ni-Ni distances (Å)		Bond angles (deg)	
Ni-O(2)	2.115(3) × 2	first neighbors	2.992 × 2		
Ni-O(1)	2.085(4) × 2		2.990 × 1	Ni-Ni-Ni	120.05
Ni-O(2)	2.104(2) × 2				119.98
Average	2.101	second			
Sum of radii [27]	2.09	neighbors	5.180 × 4	Ni-O(1)-Ni	91.63
		inlayer	5.184 × 2	Ni-O(2)-Ni	90.31
Li(1)-O(1)	2.123(11) × 2		5.154 × 2		
Li(1)-O(2)	2.262(13) × 2	interlayer	5.161 × 2		
Li(1)-O(2)	2.131(3) × 2				
Average	2.172				
Li(2)-O(1)	2.258(4) × 2				
Li(2)-O(2)	2.113(3) × 2				
Average	2.186				
Sum of radii [27]	2.16				
Sb-O(1)	1.972(4) × 2				
Sb-O(2)	1.981(5) × 4				
Average	1.976				
Sum of radii	2.00				

B. Magnetic structure

Experimental low-temperature data of neutron measurements at G4.1 are presented in Fig. 3. Additional reflections, associated with neutron magnetic scattering, appear at temperatures below 15 K. The appearance of additional reflections at low diffraction angles, especially within angles lower than the angular position of the first (001) nuclear reflection, indicates the antiferromagnetic nature of spin ordering. It should be noted that the positions of the magnetic Bragg peaks do not change in the temperature range of 1.5–15 K. The change in the magnetic scattering intensity upon decreasing temperature is associated not only with an increasing degree of magnetic ordering but also with the tilting of nickel spins. This is illustrated by the temperature dependence of the total magnetic moment and its *a*- and *c*-axis components, as shown in Fig. 4. The magnitudes and directions of the magnetic moments of $Li_3Ni_2SbO_6$ can be exactly determined from the positions and the intensities of the magnetic reflections. Results of the Rietveld analysis of neutron diffraction data at 1.5 K are shown in Fig. 5.

As a result of the profile analysis of the neutron diffraction pattern of $Li_3Ni_2SbO_6$ measured at $T = 1.5$ K, the model

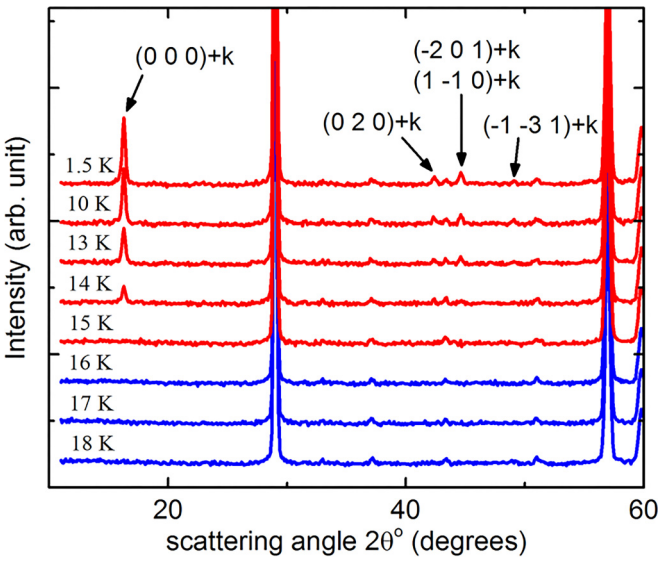

FIG. 3. A set of low-temperature neutron diffraction patterns (G4.1, $\lambda = 2.428$ Å). Arrows are pointing at the most intense additional reflections associated with magnetic scattering appearing at temperatures lower than 15 K.

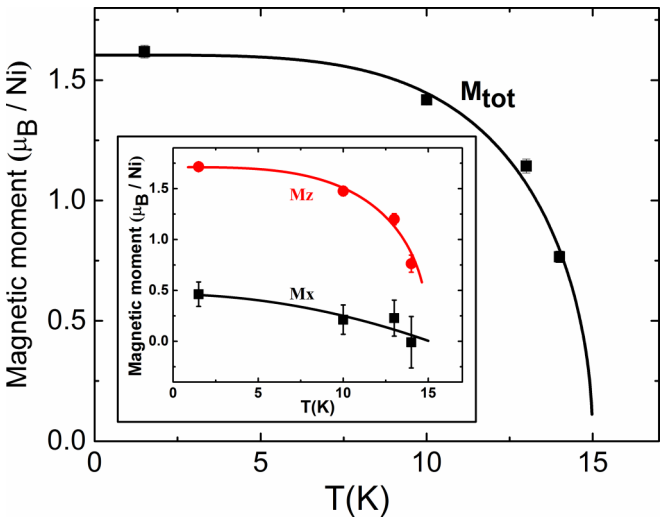

FIG. 4. Temperature dependence of the total magnetic moment as a result of the Rietveld analysis of magnetic neutron scattering at different temperatures. The components of the magnetic moment along the *a* and *c* axes are shown in the inset. Solid lines are a guide to the eye.

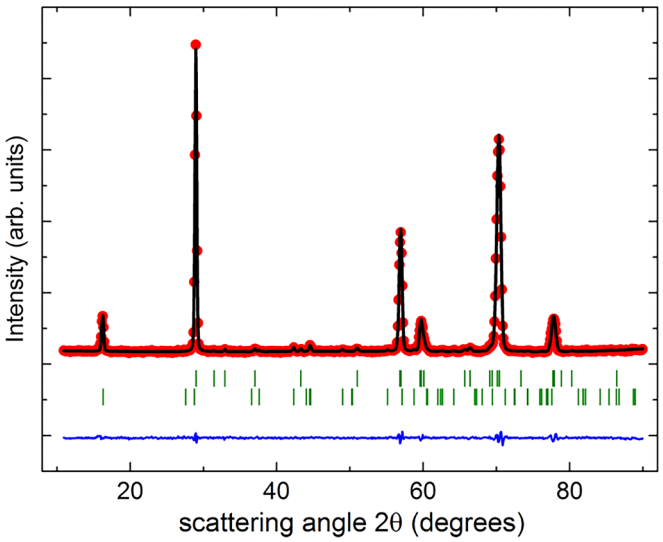

FIG. 5. Neutron diffraction pattern (G4.1, $\lambda = 2.428$ Å) of $Li_3Ni_2SbO_6$ at 1.5 K. Observed data (red dots), the calculated model (black line), and the difference (blue solid line) are shown in the 2θ region between 11° and 91°. Bragg reflections representing the atomic (top) and the magnetic structure (bottom) are given as tick marks below the observed data.

of the spin structure at complete magnetic ordering presented in Fig. 6 was constructed. The magnetic structure is commensurate across the entire temperature of long-range magnetic order, i.e., 1.5–15 K, and can be described with the propagation vector $\mathbf{k} = (1/2\ 1/2\ 0)$. That is, the magnetic unit cell is doubled along the a and b crystallographic axes in comparison to the crystallographic ones, while there is no increase of the unit cell along c.

Using the representational analysis based on the identified propagation vector and the space group $C2/m$ yields two one-dimensional magnetic irreducible representations (IR) for the Ni site. The magnetic representation Γ_{mag} is composed of two IRs:

$$\Gamma_{mag} = 3\Gamma_1^1 + 3\Gamma_2^1. \quad (1)$$

The basis vectors of these IRs (i.e., the Fourier components of the magnetization) are given in Table III. They have been calculated using the projection operator technique implemented in the BASIREPS program, included in the FULLPROF suite. Γ_1 and Γ_2 have three basis vectors each (Table III).

TABLE III. Basis vectors of two irreducible representations for propagation vector $\mathbf{k} = (1/2\ 1/2\ 0)$ and space group $C2/m$. Ni-1 and Ni-2 refer to the nonprimitive basis with coordinates (0 1/3 0) and (0 −1/3 0), respectively.

		Basis Vectors	
IRs		Ni-1	Ni-2
Γ_1	Ψ_1	(100)	(−100)
	Ψ_2	(010)	(0–10)
	Ψ_3	(001)	(00–1)
Γ_2	Ψ_1	(100)	(100)
	Ψ_2	(010)	(010)
	Ψ_3	(001)	(001)

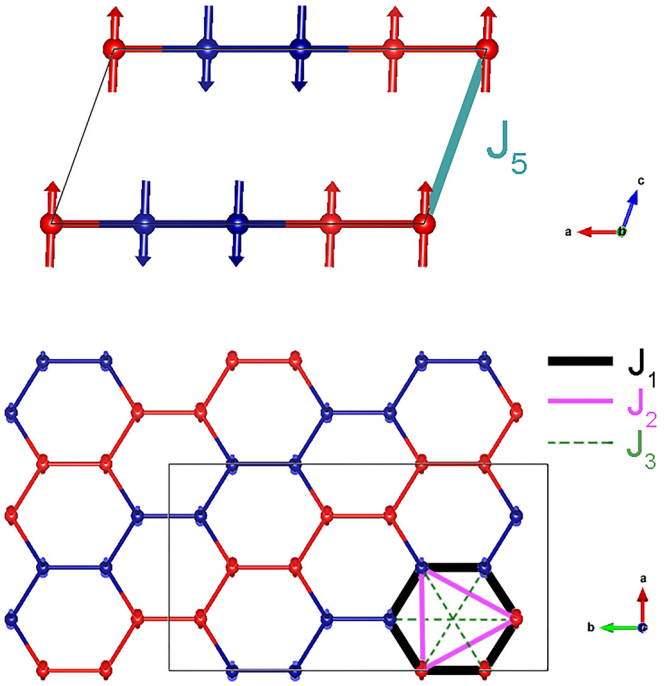

FIG. 6. Magnetic structure and exchange pathways of $Li_3Ni_2SbO_6$ at $T = 1.5$ K. The magnetic unit cell is doubled along the a and b crystallographic axes in comparison to the crystallographic one. The opposite directions of the spins are marked in different colors, i.e., red and blue. The magnetic structure can be described as zigzag ferromagnetic chains coupled antiferromagnetically in the plane and ferromagnetically along c. Notations of J_i are given according to Ref. [5].

The low-temperature long-range magnetic structure was solved through Rietveld refinement by treating the magnetic reflections as a "second phase" and including basis vector and symmetry information in the PCR file. The best refinement of the data was obtained by considering the magnetic structure associated with the irreducible representation Γ_1. In this case the magnetic moments Ni^{2+} at $T = 1.5$ K are aligned perpendicular to the crystallographic plane [ab; Fig. 6(a)].

This structure can be considered zigzag ferromagnetic chains coupled antiferromagnetically in the ab plane [Fig. 6(b)]. Interlayer interactions along the c direction are ferromagnetic. The obtained magnetic moment amounts to 1.62(2) μ_B/Ni. Its magnitude is smaller than the theoretically expected value of ∼2.0 μ_B/Ni for Ni^{2+} in the high-spin state ($S = 1$) with $g = 2.15$ [5].

C. Antiferromagnetic resonance

The temperature dependence of the ESR spectra obtained at $f = 330$ GHz illustrates the evolution of antiferromagnetic correlations in $Li_3Ni_2SbO_6$ well above the long-range ordering temperature [Fig. 7(a)]. At $T = 100$ K, a single broad resonance line is observed in the spectra. The main feature is associated with the g factor of 2.21 ± 0.03, which is slightly asymmetric and somewhat larger than $g = 2.15 \pm 0.03$ found in the X band [5]. Upon cooling, the shoulder of the resonance feature develops and slightly shifts to lower magnetic field, while the sharper main feature shows the opposite behavior.

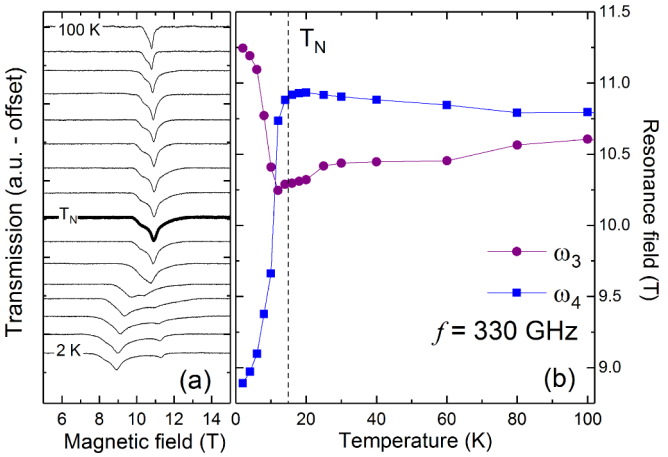

FIG. 7. (a) ESR spectra at $f = 330$ GHz in the temperature range from 100 to 2 K. The thick line marks the spectrum obtained at T_N. (b) Temperature dependence of the ω_3 and ω_4 resonance fields at $f = 330$ GHz. The dashed vertical line indicates T_N.

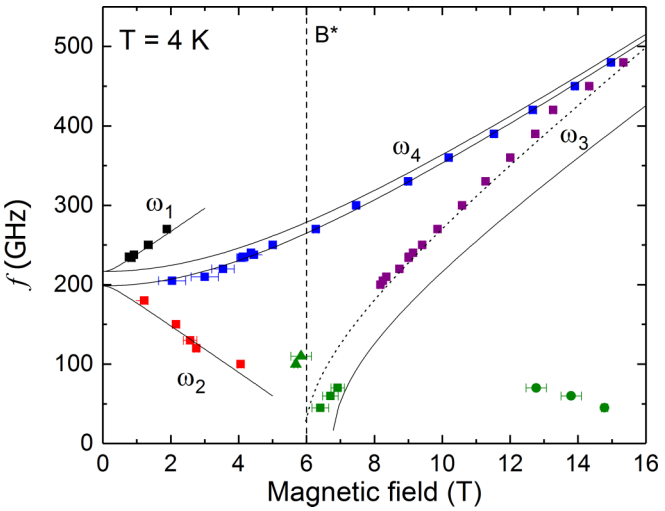

FIG. 8. Frequency vs magnetic resonance field diagram at $T = 4$ K. Colored data markers correspond to the resonances, while the solid lines show the best fit to the resonance branches ω_1 to ω_4, according to a two-sublattice model (see the text). The dotted line represents the fit to the ω_3 resonance branch with slightly different fitting parameters. B^* labels the magnetic field where M vs B starts to become nonlinear (see the text).

This is further illustrated in Fig. 7(b), which displays the temperature dependencies of the resonance fields obtained from the spectra. Around T_N, this behavior qualitatively changes as the resonance feature significantly broadens, with the sharp peak shifting to lower fields and the shoulder to higher ones. In general, this behavior implies the evolution of quasistatic internal magnetic fields; that is, it reflects the antiferromagnetic order parameter. The broad and asymmetric feature observed in the long-range antiferromagnetically ordered state where HF-ESR is susceptible to collective magnon modes is typical for antiferromagnetic resonance (AFMR) spectra in powder materials which exhibit magnetic anisotropy. As will be shown below, the two features can be associated with the AFM resonance modes ω_3 and ω_4, whose opposite behavior in external magnetic field is due to the field orientation parallel to the two different anisotropy axes. Note that the slight changes in the resonance fields below about 80 K imply the evolution of internal fields even at high temperature, i.e., the presence of short-range spin order.

Figure 8 summarizes the frequency dependence of the AFM resonance fields at $T = 4$ K, i.e., well below T_N. Most of the data points are straightforwardly attributed to four resonance branches expected in a two-sublattice model with orthorhombic anisotropy, i.e., ω_1 to ω_4, and have been color-coded accordingly. Data points with less clear assignment are shown in green. From the diagram one reads off the two zero-field splittings (ZFSs) associated with the AFMR gaps of $\Delta_{AFMR} = 198 \pm 4$ and 218 ± 4 GHz, whose small difference implies a slight orthorhombicity of the anisotropy. In addition, there is a critical field of about $B^* = 6 \pm 0.5$ T which coincides with the onset of additional contributions to the magnetic susceptibility $\partial M(B)/\partial B$ reported in Ref. [5].

AFMR branches ω_1, ω_2, and ω_4 are well described in terms of a two-AFM-sublattice model with orthorhombic anisotropy [24,25]. Even though a slightly different anisotropy field should be considered for each sublattice, a two-sublattice model agrees with the actual spin structure consisting of zigzag chains shown in Fig. 6. In the case of ω_3, there are some systematic deviations, while the general behavior is reproduced by the model. Quantitatively, the AFMR modes for a magnetic field B applied parallel to the magnetic anisotropy axis, i.e., the z axis, read

$$\frac{\omega_{z1,z2}}{\gamma} = \frac{1}{\sqrt{2}}\sqrt{2B_z^2 + C_1 + C_2 \pm \sqrt{8B_z^2(C_1 + C_2) + (C_1 - C_2)^2}}, \quad B < B_C, \tag{2}$$

$$\frac{\omega_{z3}}{\gamma} = \sqrt{B_z^2 - C_1}, \quad B > B_C. \tag{3}$$

For $B \parallel y$ axis (the second easy axis) and $B \parallel x$ axis (the hard axis), the model predicts

$$\frac{\omega_y}{\gamma} = \sqrt{B_y^2 + C_1}, \tag{4}$$

$$\frac{\omega_x}{\gamma} = \sqrt{B_x^2 + C_2}, \tag{5}$$

respectively. Here, ω and γ are the AFMR modes and the gyromagnetic ratio $\gamma = g\mu_B$, where $g = 2$, respectively. $B_i = g_i B/2$ ($i = x$, y, and z) is the modified magnetic field depending on the magnetic field direction, and $C_j = 2AK_j$ ($j = 1$ and 2 for two sublattices), where $A = B_E/M_0$ and $K_j = B_{Aj}M_0$. Here, B_E, B_{Aj}, and M_0 are the exchange field, the anisotropy field for sublattice j, and the sublattice magnetization. B_C indicates a critical field which is associated with the spin-flop field B_{SF}. Evidently, ω_1 and ω_2 correspond to $\omega_{z1,z2}$ in Eq. (2) and ω_3 to ω_{z3} [Eq. (3)] for the case of magnetic fields larger than the spin-flop field. ω_4 corresponds to ω_y in Eq. (4). ω_x, which is close to ω_y in Fig. 8, is not clearly distinguished in our ESR spectra. From the large linewidth of the ω_4 feature in whole magnetic field range, the contribution of the ω_x mode is suggested, and similar g values are estimated for both resonance modes ω_y and ω_x. The experimental data are fitted with the above equations, and the following best-fitting parameters (see the solid lines in Fig. 8) are obtained: $C_1 = 50.45 \pm 0.7\,\mathrm{T}^2$, $C_2 = 60.0 \pm 2\,\mathrm{T}^2$. The obtained g values are almost isotropic, i.e., $g_z = 2.10 \pm 0.15$, $g_y = g_x = 2.091 \pm 0.011$. Note that g_x is assumed to be similar to g_y as the linewidth of the ω_4 feature does not change significantly in the whole frequency range. For the calculation of the anisotropy field we used $B_E = 10.5 \pm 1\,\mathrm{T}$, as estimated from the saturation magnetization in the M vs B data at $T = 2\,\mathrm{K}$ [5]. The obtained anisotropy fields are $B_{A1} = 2.4 \pm 1\,\mathrm{T}$ and $B_{A2} = 2.9 \pm 1\,\mathrm{T}$. These values are close to each other, which can already be deduced from the relatively small difference between the two ZFS values.

Figure 8 shows that neither branch ω_3 nor the resonance features around B^* are well described by the plain two-sublattice model. In addition to systematic deviation of the slope at high magnetic fields, it is not obvious whether the resonances marked by green triangles and squares are assigned to ω_3. Resonances appearing at high field at $f < 100\,\mathrm{GHz}$ (green circles) are not covered by the model either. One hence has to conclude a more complex behavior beyond the simple spin-flop scenario. In order to obtain a better fit to the branch ω_3 at $B > B^*$, a larger g factor $g_z = 2.40 \pm 0.1$ would be needed (see the dotted line in Fig. 8). Although the parameters nearly coincide within the error bars with the ones describing the behavior at $B < B^*$, there is no set of parameters concomitantly describing both regimes sufficiently well. We conclude that there are either small structural changes or a change in the spin configuration at B^* which is also found in the related system $Na_3Ni_2SbO_6$ [26]. One may hence speculate that one of the competing antiferromagnetic phases reported in Ref. [5] is stabilized at $B > B^*$, so that the two-sublattice model appropriate for the AFM zigzag chains realized at low fields cannot be extended to high fields. However, the rather small deviations of the AFMR parameters from the low-field ones somehow suggest that the transition at B^* may be mainly of spin-flop nature, particularly if small additional magnetostrictive effects are considered.

IV. DISCUSSION

A combination of synchrotron and neutron diffraction techniques was used to discover the possible presence of crystal structure distortions that are extremely important (see the Introduction) in the case of honeycomb oxides. As noted previously [13] and from the present study, it follows that $Li_3Ni_2SbO_6$ has monoclinic symmetry, caused by a special stacking mode of the intrinsically hexagonal layers. This symmetry admits distortions of the structural octahedra. However, no significant distortions in NiO_6 and SbO_6 octahedra was found, as may be seen from Ni-O and Sb-O bond distances and bond angles (Table II). Moreover, the honeycomb layer, as a whole, is essentially hexagonal: for example, nonequivalent Ni-Ni distances within the layers are almost identical (Table II). Average values of Ni-O and Sb-O bond lengths are in good agreement with the sums of the corresponding Shannon's octahedral radii [27].

For further explanation of the magnetic structure, Ni-O-Ni bond angles should be considered. Both types of these angles (one for O1 and one for O2) are slightly larger than 90° due to cation-cation repulsion. According to the Goodenough-Kanamori rules, superexchange interaction via half-occupied orbitals is assumed to be ferromagnetic in the case of cation-anion angles close to 90°. In the case of honeycomb oxides this means that there are, in general, in addition to antiferromagnetic interactions, intralayer ferromagnetic interactions as, e.g., found in $Li_3Cu_2SbO_6$ with $J_{FM} = -285\,\mathrm{K}$ (Cu-O-Cu bond angle of 88.95°) and in $Na_3Cu_2SbO_6$ (95.27°) [28,12]. In $Li_3Ni_2SbO_6$, generalized gradient approximation (GGA) + U calculations indeed suggest both ferromagnetic and antiferromagnetic in-plane interactions, $J_1 = +18\,\mathrm{K}$ and $J_2 = -25\,\mathrm{K}$, respectively [5].

Another remarkable fact concerning the crystal structure of $Li_3Ni_2SbO_6$ is that the interlayer Ni-Ni distances are slightly shorter than distances between second Ni neighbors within a layer, but the magnetic interaction travels a more complex path (through an alkali metal and two oxygen atoms), and the magnitude of this interaction is less than one with the second neighbor in a layer. Furthermore, the interlayer interactions in $Li_3Ni_2SbO_6$ are slightly greater than in other related compounds with alkali cations (because lithium ions have a smaller size in comparison to other alkali-metal atoms), which leads to a smaller lattice parameter c and hence reduces the distance between the honeycomb layers ($J_5 = -2\,\mathrm{K}$ and $c = 5.15\,\text{Å}$ for $Li_3Ni_2SbO_6$ versus $J_5 = -1\,\mathrm{K}$ and $c = 5.63\,\text{Å}$ for $Na_3Ni_2SbO_6$ [5]).

The almost complete lack of lattice distortions proven by our results provides a good base for the analysis of the magnetic ground state in $Li_3Ni_2SbO_6$. The experimentally determined spin structure of ferromagnetic zigzag chains coupled antiferromagnetically within the layers confirms the theoretically predicted spin structure and is qualitatively consistent with the abovementioned coupling parameters suggested by GGA + U. Experimentally, a delicate balance between ferromagnetic and antiferromagnetic interactions is proven by the small positive value of the Weiss temperature $\Theta \sim 8\,\mathrm{K}$, which falls below the actual long-range ordering temperature $T_N = 15\,\mathrm{K}$ [5].

It should be noted that in these calculations interlayer interaction was found to be antiferromagnetic but with a negligibly small value. In contrast to theory, our neutron study shows that interlayer interactions should be ferromagnetic in the whole temperature range. This result is a consequence of considering possible magnetic structures while taking into

account the space group $C2/m$ and the propagation vector $\mathbf{k} = (1/2\ 1/2\ 0)$. In addition, our neutron measurements imply a very interesting phenomenon, namely, a certain tilt of magnetic moments in the ordered state and the change of this tilting with temperature. The tilting manifests in the appearance of a small magnetic moment component along the a axis (M_x) which increases somehow with the magnetic order parameter upon cooling (see the inset in Fig. 4). Thus, we have observed that Ni spins, directed along the crystallographic c axis at temperatures just below the Néel temperature of 15 K, incline with a further decrease in temperature and finally become stabilized perpendicular to the honeycomb Ni_2SbO_6 layers. As a result, the total tilt angle of the nickel magnetic moments is 15.6°. Based on the present data, the general behavior and the tilt angles at 1.5 K as well as just below T_N are derived. Whether the evolution of ordered nickel spins inclination in the temperature regime 1.5–10 K appears gradual or abrupt requires additional examination. The observed alignment of the magnetic moments perpendicular to the ab plane (see Fig. 5) at $T = 1.5$ K is in agreement with suggestions based on previous ^{7}Li ($I = 3/2$) NMR data and with spin-polarized density-functional-theory (DFT) calculations [5].

Our data imply a reduced value of the magnetic moment, i.e., 1.62(2) μ_B/Ni. This is in agreement with significant magnetic frustration of the long-range interactions in this system which is already evident if the nearest- and next-nearest-neighbor couplings J_1 and J_2 are considered. On the other hand, such reduced magnitude of the magnetic moment may be associated with stacking faults. Violation of long-range ordering takes place with every fault appearing in the system. As a result, a nonideal layer arrangement diminishes the intensities of magnetic peaks so that the measured value of the ordered moment is lower than expected. Such behavior was observed earlier in $Cu_3Ni_2SbO_6$ and $Cu_3Co_2SbO_6$ [4].

The low-energy magnetic excitations probed by HF-ESR imply a two-sublattice model in full agreement with the spin structure found in the neutron experiments. The zero-field gaps amount to $\Delta = 198 \pm 4$ and 218 ± 4 GHz, indicating a significant anisotropy field, which is typical for a system with Ni^{2+} ions in a slightly distorted octahedral environment due to single-ion effects. The g factor shows no significant anisotropy. The observation of an asymmetrically broadened ESR line at high temperatures further confirms the presence of axial anisotropy with slight orthorhombicity. The shift of the resonance lines upon cooling suggests the evolution of short-range antiferromagnetic order below about 80 K, i.e., more than 5 times T_N. The evolution of local magnetic fields far above T_N further confirms the scenario of a magnetically rather two-dimensional and frustrated system. The development of the internal magnetic field below T_N which is shown by the splitting of the AFMR lines follows the order parameter obtained from the analysis of the antiferromagnetic Bragg peaks in Fig. 4. The analysis of the data in the minimal two-sublattice model yields the anisotropy fields in $Li_3Ni_2SbO_6$. The results imply strong AFM interactions, corroborating the neutron data and previous DFT results [5].

V. CONCLUSIONS

Using a combination of high-resolution synchrotron and neutron powder diffraction, the $C2/m$ model of $Li_3Ni_2SbO_6$ has been confirmed and refined. The effect of stacking faults on the crystal structure is not negligible and requires careful examination. The ground-state spin configuration of $Li_3Ni_2SbO_6$ below $T_N = 15$ K has been determined. It represents a commensurate antiferromagnetic zigzag structure with propagation vector $\mathbf{k} = (1/2\ 1/2\ 0)$. It is also remarkable that the coupling between magnetically active layers has a ferromagnetic nature, in contrast to theoretical predictions. Below T_N, the magnetic moments demonstrate significant tilting from the crystallographic c direction, and at the lowest reached temperature, $T = 1.5$ K, it reaches its maximal value of 15.6°, with moments aligned perpendicular to the honeycomb (001) crystallographic plane. The low-energy excitations probed by the AFMR study are in agreement with the two-sublattice model derived from the neutron data. Furthermore, the axial anisotropy with the orthorhombicity showing up in zero-field gaps of $\Delta = 198 \pm 4$ and 218 ± 4 GHz has been quantitatively analyzed. Above T_N, we found short-range antiferromagnetic order up to about 80 K.

ACKNOWLEDGMENTS

The reported study was funded by Russian Foundation for Basic Research according to Research Projects No. 14-03-01122, No. 14-02-00245 (E.A.Z. and V.B.N.), No. 17-52-45014 (E.A.Z.), and No. 16-02-00360 (A.I.K., S.Yu.P., A.N.K., and A.L.M.). R.K. and E.A.Z. acknowledge financial support from the Excellence Initiative of the German Federal Government and States. E.A.Z. acknowledges support of the Russian Science Foundation through the Project No. 17-12-01207.

[1] L. P. Regnault and J. Rossat-Mignod, Magnetic Properties of Layered Transition Metal Compounds, in *Phase Transitions in Quasi-Two-Dimensional Planar Magnets*, edited by L. J. De Jongh (Kluwer Academic, Dordrecht, 1990), pp. 271–321.

[2] L. Viciu, Q. Huang, E. Morosan, H. W. Zandbergen, N. I. Greenbaum, T. McQueen, and R. J. Cava, Structure and basic magnetic properties of the honeycomb lattice compounds $Na_2Co_2TeO_6$ and $Na_3Co_2SbO_6$, J. Solid State Chem. **180**, 1060 (2007).

[3] P. H. Y. Li, R. F. Bishop, D. J. J. Farnell, and C. E. Campbell, Phase diagram of a frustrated Heisenberg antiferromagnet on the honeycomb lattice: The J_1-J_2-J_3 model, Phys. Rev. B **86**, 144404 (2012).

[4] J. H. Roudebush, N. H. Andersen, R. Ramlau, V. O. Garlea, R. Toft-Petersen, P. Norby, R. Schneider, J. N. Hay, and R. J. Cava, Structure and magnetic properties of $Cu_3Ni_2SbO_6$ and $Cu_3Co_2SbO_6$ delafossites with honeycomb lattices, Inorg. Chem. **52**6083 (2013).

[5] E. A. Zvereva, M. I. Stratan, Y. A. Ovchenkov, V. B. Nalbandyan, J.-Y. Lin, E. L. Vavilova, M. F. Iakovleva, M. Abdel-Hafiez, A. V. Silhanek, X.-J. Chen, A. Stroppa, S. Picozzi, H. O. Jeschke, R. Valentí, and A. N. Vasiliev, Zigzag antiferromagnetic quantum ground state in monoclinic honeycomb lattice antimonates $A_3Ni_2SbO_6$ (A = Li, Na), Phys. Rev. B **92**, 144401 (2015).

[6] N. Bhardwaj, A. Gupta, and S. Uma, Evidence of cationic mixing and ordering in the honeycomb layer of Li_4MSbO_6 (M(III) = Cr, Mn, Al, Ga) (s.g. C2/c) oxides, Dalton Trans. **43**, 12050 (2014).

[7] W. Schmidt, R. Berthelot, L. Etienne, A. Wattiaux, and M. A. Subramanian, Synthesis and characterization of O3-$Na_3LiFeSbO_6$: A new honeycomb ordered layered oxide, Mater. Res. Bull. **50**, 292 (2014).

[8] J. Xu, A. Assoud, N. Soheilnia, S. Derakhshan, H. L. Cuthbert, J. E. Greedan, M. H. Whangbo, and H. Kleinke, Synthesis, structure, and magnetic properties of the layered copper (II) oxide $Na_2Cu_2TeO_6$, Inorg. Chem. **44**, 5042 (2005).

[9] S. Derakhshan, H. L. Cuthbert, J. E. Greedan, B. Rahaman, and T. Saha-Dasgupta, Electronic structures and low-dimensional magnetic properties of the ordered rocksalt oxides $Na_3Cu_2SbO_6$ and $Na_2Cu_2TeO_6$, Phys. Rev. B **76**, 104403 (2007).

[10] Y. Miura, R. Hirai, T. Fujita, Y. Kobayashi, and M. Sato, Spin-gap behavior of distorted honeycomb lattice system $Na_3Cu_2SbO_6$, J. Magn. Magn. Mater. **310**, e389 (2007).

[11] C. N. Kuo, T. S. Jian, and C. S. Lue, Characterization of the spin gap nature in $Na_3Cu_2SbO_6$ using ^{23}Na NMR, J. Alloys Comp. **531**, 1 (2012).

[12] M. Schmitt, O. Janson, S. Golbs, M. Schmidt, W. Schnelle, J. Richter, and H. Rosner, Microscopic magnetic modeling for the $S = 1/2$ alternating-chain compounds $Na_3Cu_2SbO_6$ and $Na_2Cu_2TeO_6$, Phys. Rev. B **89**, 174403 (2014).

[13] E. A. Zvereva, M. A. Evstigneeva, V. B. Nalbandyan, O. A. Savelieva, S. A. Ibragimov, O. S. Volkova, L. I. Medvedeva, A. N. Vasiliev, R. Klingeler, and B. Büchner, Monoclinic honeycomb-layered compound $Li_3Ni_2SbO_6$: Preparation, crystal structure and magnetic properties, Dalton Trans. **41**, 572 (2012).

[14] J. Rodriguez-Carvajal, Recent advances in magnetic structure determination by neutron powder diffraction, Phys. B (Amsterdam, Neth.) **192**, 55 (1993).

[15] FULLPROF suite, http://www.ill.eu/sites/fullprof/.

[16] P. Comba, M. Großhauser, R. Klingeler, C. Koo, Y. Lan, D. Muller, J. Park, A. Powell, M. J. Riley, and H. Wadepohl, Magnetic interactions in a series of homodinuclear lanthanide complexes, Inorg. Chem. **54**, 11247 (2015).

[17] J. M. Paulsen, R. A. Donaberger, and J. R. Dahn, Layered T^2-, O^6-, O^2-, and P2-type $A_{2/3}$ $[M'^{2+}_{1/3}M^{4+}_{2/3}]O_2$ bronzes, A = Li, Na; M' = Ni, Mg; M = Mn, Ti, Chem. Mater. **12**, 2257 (2000).

[18] M. Trömel, and J. Hauck, Über fehlordnung in gittern vom Li_2SnO_3-typ und die tieftemperaturform dieser verbindung, Z. Anorg. Allg. Chem. **373**, 8 (1970).

[19] V. V. Politaev, V. B. Nalbandyan, A. A. Petrenko, I. L. Shukaev, V. A. Volotchaev, and B. S. Medvedev, Mixed oxides of sodium, antimony (5+) and divalent metals (Ni, Co, Zn or Mg), J. Solid State Chem. **183**, 684 (2010).

[20] J. Ma, S.-H. Bo, L. Wu, Y. Zhu, C. P. Grey, and P. G. Khalifah, Ordered and disordered polymorphs of $Na(Ni_{2/3}Sb_{1/3})O_2$: Honeycomb-ordered cathodes for Na-ion batteries, Chem. Mater. **27**, 2387 (2015).

[21] E. A. Zvereva, M. I. Stratan, A. V. Ushakov, V. B. Nalbandyan, I. L. Shukaev, A. V. Silhanek, M. Abdel-Hafiez, S. V. Streltsov, and A. N. Vasiliev, Orbitally induced hierarchy of exchange interactions in the zigzag antiferromagnetic state of honeycomb silver delafossite $Ag_3Co_2SbO_6$, Dalton Trans. **45**, 7373 (2016).

[22] O. A. Smirnova, V. B. Nalbandyan, A. A. Petrenko, and M. Avdeev, Subsolidus phase relations in Na_2O-CuO-Sb_2O_n system and crystal structure of new sodium copper antimonate $Na_3Cu_2SbO_6$, J. Solid State Chem. **178**, 1165 (2005).

[23] P. W. Stephens, Phenomenological model of anisotropic peak broadening in powder diffraction, J. Appl. Crystallogr. **32**, 281 (1999).

[24] T. Nagamiya, K. Yoshida, and R. Kubo, Antiferromagnetism, Adv. Phys. **4**, 1 (1955).

[25] M. Hase, M. Hagiwara, and K. Katsumata, Observation of an antiferromagnetic resonance in the spin-Peierls compound $CuGeO_3$ doped with Zn, Phys. Rev. B **54**, R3722 (1996).

[26] J. Werner, W. Hergett, M. Gertig, J. Park, C. Koo, and R. Klingeler, Anisotropy governed competition of magnetic phases in the honeycomb quantum magnet $Na_3Ni_2SbO_6$ studied by dilatometry and high-frequency ESR, Phys. Rev. B **95**, 214414 (2017).

[27] R. D. Shannon, Revised effective ionic radii and systematic studies of interatomic distances in halides and chalcogenides, Acta Crystallogr. **A32**, 751 (1976).

[28] C. Koo, E. A. Zvereva, I. L. Shukaev, M. Richter, M. I. Stratan, A. N. Vasiliev, V. B. Nalbandyan, and R. Klingeler, Static and dynamic magnetic response of fragmented haldane-like spin chains in layered $Li_3Cu_2SbO_6$, J. Phys. Soc. Jpn. **85**, 084702 (2016).